RSC Advances

ROYAL SOCIETY OF CHEMISTRY

www.rsc.org/advances

Journal Name

ARTICLE TYPE

Cite this: DOI: 10.1039/xxxxxxxxxx

The Effect of Nitrido, Azide, and Nitrosyl Ligands on Magnetization Densities and Magnetic Properties of Iridium PNP Pincer-Type Complexes†

Daniel Stuart,[a,b] Paweł Tecmer,[a,c*] Paul W. Ayers,[a] and Katharina Boguslawski[c*]

Received Date
Accepted Date

DOI: 10.1039/xxxxxxxxxx

www.rsc.org/journalname

We present a systematic theoretical study of electronic structures, magnetization densities, and magnetic properties of iridium PNP pincer-type complexes containing non-innocent nitrido, azide, and nitrosyl ligands. Specifically, the quality and accuracy of density functional theory (DFT) in predicting magnetization densities obtained from various approximate exchange–correlation functionals is assessed by comparing them to complete active space self-consistent field (CASSCF) reference distributions. Our analysis points to qualitative differences in DFT magnetization densities at the iridium metal center and the pincer ligand backbone compared to CASSCF reference data when the non-innocent ligands are changed from nitrido, to azide, to nitrosyl. These observations are reflected in large differences in hyperfine couplings calculated for the iridium metal center.

1 Introduction

Transition metal complexes are central to metal-mediated catalysis and bioinorganic chemistry. Specifically, there has been a great deal of research into the role of nitrido complexes in a wide array of applications including catalysis in biological systems and the Haber–Bosch process. Currently, the group 8 ruthenium and iron terminal nitrido complexes are considered active catalysts in reactions involving nitrogen fixation and C-H bond activation.[1–4] Looking at bioinorganic systems, terminal nitrido complexes can play a vital role in enzymatic reactions and using a model system can provide insight into the mechanism and role the nitrido ligand plays in the body. High-valent nitrido iron species have been proposed as intermediates in some of these reactions leading to unusually high formal oxidation states of the iron metal center.[5] The first terminal $Fe^{IV} \equiv N$ complex was synthesized in solution at room temperature and has been fully characterized by ^{1}H-, ^{31}P-, ^{15}N-NMR, Mössbauer, infrared, and X-ray absorption spectroscopy showing a relatively short Fe-N distance compared to the Fe^{IV}-O bond lengths of oxoiron(IV) complexes commonly seen in the catalytic cycles of heme and nonheme iron enzymes.[6–9] This was explained by the greater π basicity of the nitrido ligand compared to the oxo ligand.

The nitrido ligand can be thought of as a N^{3-} trianionic ligand with a significant charge transfer generally resulting in the metal center having a higher oxidation state. Since ruthenium and osmium transition metals can adopt an oxidation state of $+6$ or higher, it is more common to find examples of these nitrido compounds.[3] Going further, there are more examples of osmium nitrido complexes than their ruthenium analogs. A variety of ligands have been used to support these osmium compounds ranging from halogen and pseudohalogen ligands, amines, alkoxides, polypropyl ligands, and polyoxometallates. One important ligand commonly used to stabilize these nitrido complexes is the PNP pincer ligands which are commonly known to act as active catalysts in hydrogenation and dehydrogenation reactions.[10–18] Recently there has been a push to investigate the PNP-type pincer complexes of first row, inexpensive metals such as cobalt[18] and iron[14] compared to the ruthenium, rhodium, and iridium counterparts which have already proven to be useful catalysts. In a recent study, a rare Re(I) PNP pincer complex was used for activation of nitriles involving reversible C–C and M–N bond formation.[19] In another study, the square-planar Ir(II) PNP pincer complex [IrCl(L)] (where $L = N(CH_2CH_2PR_2)_2$ and $R = tBu$) was isolated and then oxidized to give the first example of the diamagnetic $[IrCl(L)]PF_6$ square-planar iridium(III) complex.[20]

---

* Corresponding authors: E-mails: katharina.boguslawski@gmail.com, ptecmer@gmail.com.

[a] *Department of Chemistry and Chemical Biology, McMaster University, 1280 Main Street West, Hamilton, L8S 4M1, Ontario, Canada.*

[b] *Department of Chemistry and Biochemistry, University of Lethbridge, 4401 University Drive, Lethbridge, Alberta, T1K 3M4, Canada.*

[c] *Institute of Physics, Faculty of Physics, Astronomy and Informatics, Nicolaus Copernicus University, Grudziądzka 5, 87-100 Toruń, Poland.*

† Electronic Supplementary Information (ESI) available: BP86-optimized molecular structures, DFT and CASSCF magnetization density isosurface plots, DFT–CASSCF and CASSCF–CASSCF magnetization density difference plots, CASSCF natural orbitals and natural occupation numbers, and $\langle S^2 \rangle$ expectation values. See DOI: 10.1039/b000000x/

The reactivity of metal terminal nitrido complexes were considered rare, primarily due to unfavourable electron interactions between strong π-donor ligands and electron rich metals. More specifically, those metal nitrido complexes with a valence-electron count of d^n where $n \geq 4$, are considered unstable because of the inability for M–N π-bonding to occur due to the absence of free metal orbitals.[3] Recently, it has been shown that square planar terminal nitrido d^4 complexes can exist as a result of the two free d-orbitals with appropriate symmetry, analogous to a d^2 pseudo-octahedral complex.[21] An example of this includes a transient rhodium(IV) terminal nitrido complex, synthesized from the azido analog, stabilized by the pincer complex $N(CH_2CH_2PR_2)_2$ (where R = tBu).[22] The unpaired electron is primarily localized in a Rh–N π^*-orbital leading to a covalent-like bond with substantial spin density located at the nitrido ligand. A similar iridium nitrido complex was previously synthesized,[22] and was characterized by Electron Paramagnetic Resonance (EPR) studies with the aid of density functional theory (DFT) calculations. It was also noted in both the iridium and rhodium complexes that dimerization occurred via radial-type N–N coupling.

Another important ligand in biological and industrial processes is the nitrosyl ligand. Transition metal nitrosyl ligand complexes often play an important role in homogeneous catalysis in enzymatic reactions of biological systems but are relatively unexplored for other applications. They function as π accepting, non-innocent ancillary ligands and take the form of either the linear or bent transformations. Since these configurations are reversible, being able to bind as either NO^+, $NO^\bullet$, or NO^- can trigger various catalytic pathways. The non-innocence of this ligand allows it to stabilize various species involved in catalysis by either supplying electron density to the metal center or scavenging electrons located on the metal center.[23–25] The NO ligand also functions as a redox-active ligand responsible for oxygen atom transfer via the nitric oxide and nitrosyl redox couple.[26]

Unfortunately, experimental studies on transition metal compounds are often not sufficient to determine their molecular properties, like, for instance, spatial distributions of (unpaired electron) spin density in the ground state and energy differences between states of different spin multiplicity. As complement to experimental studies, theoretical modeling of transition metal complexes has thus become indispensable for a detailed understanding of their molecular properties, function as catalytically active centers, and catalytic mechanisms. However, theoretical determination of electronic structures and properties of transition-metal compounds remains a remarkable challenge for present-day quantum chemistry, especially if transition-metal complexes contain unpaired electrons and hence have to be described by open-shell wavefunctions.[27,28] Computationally cheap methods such as DFT, often fail in predicting the energetically lowest-lying spin-state electronic configuration and spin-density distributions in open-shell transition-metal complexes.[23,24,29–37] Failures of approximate exchange–correlation functionals in predicting molecular properties of open-shell complexes have been traced to the delocalization error and static correlation error,[38,39] which are rooted in an inappropriate behavior of the energy with respect to fractional charges and fractional spins.[40–44] Reliable modeling of transition metal compounds requires more expensive, but robust wavefunction-based methods that can further be used to assess the accuracy and reliability of DFT calculations. Yet, due to the large size of catalytically active transition-metal complexes, wavefunction-based methods are prohibitive for routine applications and DFT calculations are commonly used to elucidate molecular properties and confirm experimental findings. In this work, we use wavefunction-based methods to investigate the electronic structure of iridium PNP pincer-type complexes with nitrido (**1**), azide (**2**), and nitrosyl (**3**) ligands, as shown in Figure 1, and examine how those ligands influence the electronic structure and magnetic properties of iridium complexes. Our wavefunction calculations will serve as a reference to assess the accuracy and reliability of commonly used approximate exchange–correlation functionals in predicting ground-state properties of iridium compounds.

This work is organized as follow. In section 2, we summarize the computational methodology used to optimize geometries, electronic structures, and magnetic properties of iridium nitrido, azide, and nitrosyl complexes. Numerical results are presented in section 3. Finally, we conclude in section 4.

2 Computational Methodology

2.1 DFT

All unrestricted DFT calculations were performed with the quantum chemical package ADF 2013 (Amsterdam Density Functional).[45] The structures of **1**, **2**, and **3** were optimized using the triple-ζ polarization Slater-type orbital basis set (TZP) along with the BP86 exchange–correlation functional.[46,47] No spatial symmetry constraints were imposed during the optimization process. The overall electronic charge of compounds **1** and **2** is neutral and both molecules are in the doublet (S = 1/2) electronic ground state. Compound **3** has a molecular charge of +1 and a triplet (S = 1) ground-state electronic configuration. A large frozen core was used. Since the effect of spin-orbit coupling on molecular geometries is negligible, only scalar-relativistic effects were included through the zeroth-order regular approximation (ZORA) Hamiltonian.[48]

These optimized geometries were used in subsequent single-point calculations to determine magnetization-density distributions using the B3LYP,[49] BLYP,[47,50] BP86,[46,47] M06-L,[51,52] OLYP,[53] OPBE,[54] PBE,[54] PBE0,[55,56] TPSS,[57] and TPSSh[58] exchange–correlation functionals. In these single-point calculations, no frozen core was used. We should note that in all DFT calculations no spin contamination was observed and all $\langle S^2 \rangle$ expectation values agree very well with the corresponding ideal value. All $\langle S^2 \rangle$ expectation values are summarized in Table S4 of the Supplementary Information. †

The g tensors[59] and the nuclear magnetic dipole hyperfine interactions (A tensors)[60] were calculated for the BP86[46,47] and B3LYP[49] exchange–correlation functionals. The Gaussian-type nuclear model was used, while spin–orbit coupling was included using the all-electron ZORA Hamiltonian and was treated in a self-consistent manner.

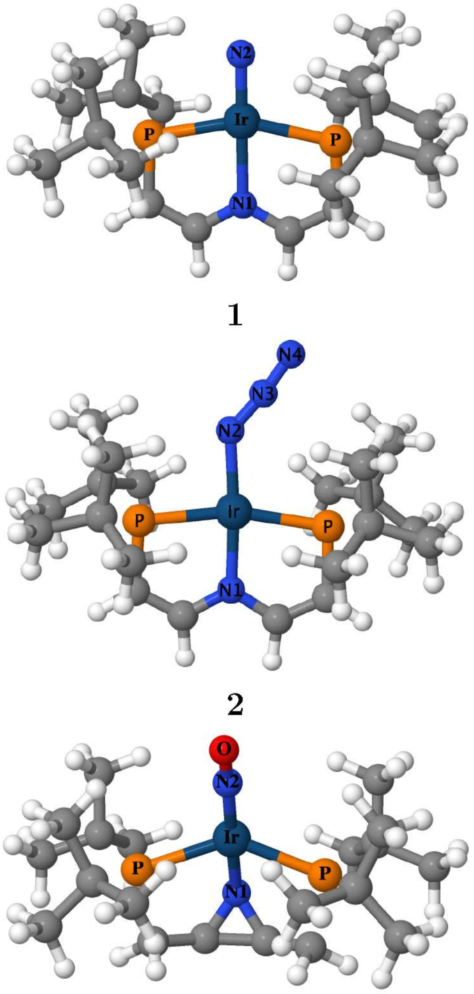

1

2

3

Fig. 1 BP86 optimized structures of iridium PNP pincer-type complexes. **1**: IrLN. **2**: $IrLN_3$. **3** IrLNO. L = $(N(CH_2CH_2PR_2)_2)$ and R = tBu.

2.2 CASSCF

All CASSCF[61–63] calculations were performed in the MOLPRO2012 program package[64] using the DFT optimized structures. A TZP ANO-RCC basis set was used for the iridium atom and a DZ ANO-RCC basis set for all other elements. Specifically, the following contraction schemes were applied: H:$(8s4p3d1f) \rightarrow [3s2p1d]$,[65] C, N, and O:$(8s7p4d3f2g) \rightarrow [3s3p1d]$,[66] P:$(8s7p5d4f2g) \rightarrow [4s3p1d]$,[66] and Ir:$(11s8p6d4f2g) \rightarrow [7s6p3d2f]$.[67] Scalar relativistic effects were included through the second-order Douglas–Kroll–Hess Hamiltonian.[68,69] In all CASSCF calculations, no spatial symmetry was imposed. However, to facilitate chemical interpretation, we will label the orbitals according to their main character (σ, π, etc) whenever possible. The natural orbitals of all CASSCF calculations and their corresponding natural occupation numbers are listed in Figures S4 and S5, S9 to S13, and S17 to S19 of the Supplementary Information.

For complex **1**, we performed two sets of CASSCF calculations, CAS(9,8)SCF and CAS(9,10)SCF. The former one comprises two doubly occupied π-type orbitals, one doubly occupied σ-type orbital, one singly occupied π^*-type orbital, one virtual π^*-type orbital, one virtual σ^*-type orbital and one additional virtual orbital. The active space in CAS(9,10)SCF additionally contains two virtual orbitals (see Figures S4 and S5 of the Supplementary Information for more details). This largest active space calculation will be used as reference data for system **1**.

The minimal active space for system **2** comprises two doubly occupied π-type orbitals, two unoccupied π^*-type orbitals as well as one singly occupied π-type orbital (CAS(5,5)SCF). This active space was further extended by one and two sets of occupied and virtual orbitals, resulting in CAS(7,7)SCF and CAS(9,9)SCF, respectively. In another series, we included only occupied orbitals in the CAS(5,5) active space leading to our CAS(9,7)SCF and CAS(13,9)SCF calculations. The largest active space was composed of 15 electrons and 11 orbitals, resulting in CAS(15,11)SCF (see Figures S9 to S13 of the Supplementary Information for more details). Specifically, it contains seven doubly occupied π/π^*-type orbitals, one singly occupied π-type orbital, and three virtual orbitals (two π^*/π^*-type orbitals and one "double-*d* shell" orbital). The latter was used as reference calculation for complex **2**.

For complex **3**, we performed CAS(6,6)SCF calculations, where 6 electrons were correlated among 6 orbitals. The active space includes two doubly occupied π^*-type orbitals, two virtual π^*-type orbitals, and two singly occupied σ-type orbitals. In a subsequent calculations, we extended the active spaces to CAS(8,8)SCF and CAS(10,10)SCF, where one and two sets of additional π^*-type orbitals were correlated. Our final active space was extended by two virtual "double-*d* shell" orbitals, resulting in CAS(10,12)SCF. This calculation was used as a reference calculation for **3** (see Figures S17 to S19 of the Supplementary Information for more details).

Table 1 Absolute error and root-square error of DFT–CASSCF and CASSCF–CASSCF magnetization density difference distributions for complexes **1**, **2**, and **3**. CASSCF indicates the errors in magnetization densities calculated from the largest active space and the second largest active space as summarized in the Computational Details.

Method	**1**		**2**		**3**	
	Δ_{abs}	Δ_{rs}	Δ_{abs}	Δ_{rs}	Δ_{abs}	Δ_{rs}
BP86	0.175	0.019	0.419	0.048	0.451	0.043
BLYP	0.158	0.017	0.412	0.048	0.454	0.044
OLYP	0.187	0.020	0.415	0.046	0.469	0.045
OPBE	0.187	0.020	0.420	0.046	0.465	0.045
PBE	0.170	0.018	0.411	0.047	0.449	0.043
PBE0	0.180	0.020	0.331	0.031	0.577	0.062
TPSS	0.177	0.019	0.432	0.047	0.457	0.044
TPSSh	0.181	0.020	0.398	0.040	0.496	0.050
M06-L	0.152	0.013	0.398	0.040	0.480	0.045
B3LYP	0.162	0.018	0.348	0.034	0.540	0.057
CASSCF	0.028	0.005	0.005	0.001	0.013	0.002

3 Numerical Results

3.1 Magnetization density distributions

To assess the similarity of different magnetization densities, we need to define suitable measures. This will allow us, for instance, to assess the accuracy of a given magnetization density with respect to a reference magnetization density. Isosorface plots of the magnetization density or the difference in magnetization densi-

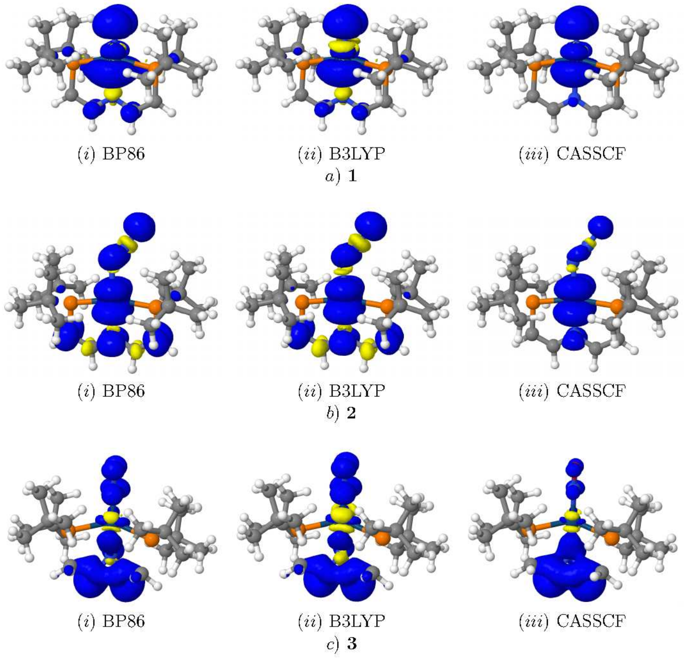
(i) BP86 (ii) B3LYP (iii) CASSCF
a) 1

(i) BP86 (ii) B3LYP (iii) CASSCF
b) 2

(i) BP86 (ii) B3LYP (iii) CASSCF
c) 3

Fig. 2 Magnetization density plots of a) complex **1** with an isosurface value of 0.001, b) complex **2** with an isosurface value of 0.001, and c) complex **3** with an isosurface value of 0.003, comparing the (i) BP86 and (ii) B3LYP exchange-correlation functionals with the (iii) CASSCF method. A blue isosurface indicates an excess of α-electron density, while a yellow isosurface indicates an excess of β-electron density.

ties calculated for two different quantum chemistry methods can only serve as a qualitative measure. A better way to evaluate the similarity in these methods is to introduce a distance measure that quantifies the errors between two magnetization densities. Our distance measures are defined with respect to the absolute error in the magnetization density difference distribution (for either the same quantum chemistry method or two different methods). Specifically, the accumulated absolute error Δ_{abs} is defined as

$$\Delta_{\text{abs}} = \int |\rho_1^{\text{m}}(\mathbf{r}) - \rho_2^{\text{m}}(\mathbf{r})| d\mathbf{r} \tag{1}$$

and the root-square error Δ_{rs} reads

$$\Delta_{\text{rs}} = \sqrt{\int |\rho_1^{\text{m}}(\mathbf{r}) - \rho_2^{\text{m}}(\mathbf{r})|^2 d\mathbf{r}} \tag{2}$$

where $\rho_i^{\text{m}}(\mathbf{r})$ is the magnetization density distriubtion of some calculation i (either CASSCF or DFT). If two magnetization densities $\rho_i^{\text{m}}(\mathbf{r})$ and $\rho_j^{\text{m}}(\mathbf{r})$ are similar, both error measures Δ_{abs} and Δ_{rs} will approach zero.

3.1.1 Complex 1—Nitrido.

The magnetization-density distributions calculated for **1** are shown in Figure 2(a) for an isosurface value of 0.001. We should emphasize that, for all iridium complexes, all investigated exchange–correlation functionals give magnetization-density distributions that can be arranged in two main groups: those that yield magnetization densities qualitatively closer to BP86 and those being closer to B3LYP. Hence only the BP86 and B3LYP results are shown in Figure 2. The magnetization density distributions of the remaining exchange–correlation functionals as well as all CASSCF magnetization densities are summarized in the Supplementary Information. Specifically, the differences in CASSCF magnetization densities optimized for various active spaces are negligible and thus only the CAS(9,10)SCF results are shown (see Table 1 and Supplementary Figure S1). Furthermore, an analysis of the CASSCF wavefunction indicates a single-reference nature of system **1** (large (absolute) CI expansion coefficients of the principal configuration of 0.97 and $|\text{CI}|^2 = 0.95$ for CAS(9,10)SCF).

For both DFT and CASSCF, an excess of α-electron density exists on the nitrido ligand and iridium metal center (see Figure 2(a) and Supplementary Figure S2). There appears to be nearly no spin density on the PNP pincer ligand in CASSCF, however, DFT predicts there to be an excess of β-density on the nitrogen atoms in complex **1**. Furthermore, compared to CASSCF, DFT predicts the α-electron density to be more delocalized around the iridium metal and carbon atoms of the PNP pincer ligand backbone. The DFT–CASSCF difference plots (see Supplementary Figure S3), illustrate there is an excess of α-electron density around the iridium metal center in CASSCF compared to DFT calculations. The magnetization density predicted by the PBE, BP86, and BLYP exchange–correlation functionals are qualitatively the closest match to the CAS(9,10)SCF reference magnetization density, whereas the hybrid functionals PBE0, B3LYP, and TPSSh show a clear separation of α- and β-electron density around the metal center and the PNP pincer backbone and are not in good agreement with CAS(9,10)SCF results.

The absolute error and root-square error for all DFT–CASSCF magnetization density difference distributions are summarized in Table 1. Although PBE, BP86, and BLYP yield magnetization densities that qualitatively agree best with the CASSCF reference distribution (lack of β-electron density around the metal center), they have the largest Δ_{abs} and Δ_{rs} values for all investigated exchange–correlation functionals. The smallest errors in magnetization density are found for the M06-L and B3LYP exchange–correlation functionals, even though the corresponding magnetization density distributions differ qualitatively from the CASSCF reference. Note, however, that the differences in Δ_{abs} and Δ_{rs} are small and it remains difficult to judge which exchange–correlation functionals predict the most accurate magnetization densities.

3.1.2 Complex 2—Azide.

The magnetization density distributions of compound **2** are shown in Figure 2(b) with an isosurface value of 0.001. All our CASSCF calculations, *i.e.*, CAS(5,5)SCF, CAS(7,7)SCF, CAS(9,9)SCF, CAS(13,9)SCF, and CAS(15,11)SCF, predict similar magnetization density distributions, with differences being negligible and much smaller than the differences between DFT and CASSCF results. Thus only the CAS(15,11)SCF magnetization density is shown in Figure 2(b) (for a complete picture, we refer the reader to Figure S6 in the Supplementary Information). Furthermore, an analysis of the CASSCF wavefunction indicates a single-reference nature of complex **2** (large (absolute) CI expansion coefficients of the principal configuration of 0.97 and $|\text{CI}|^2 = 0.95$).

In general, there is an excess of α-electron density around the iridium metal center and the nitrogen atoms of both the azide and PNP pincer ligands for both DFT and CASSCF (see Figure 2(b) and Supplementary Figure S7). The DFT–CASSCF magnetization density difference plots show the iridium atom carrying less α-electron density in CASSCF compared to the DFT results (see Supplementary Figure S8). Looking at the carbon atoms on the PNP pincer ligand backbone, we observe a noticeable difference in the magnetization density distributions predicted by DFT and CASSCF. While DFT shows alternating excess of α- and β-electron density on the C-C-N-C-C backbone, respectively, CAS(15,11)SCF results in α-electron density only on the nitrogen atom of the ligand backbone and no β-electron density, independent of the active space chosen in CASSCF calculations. Furthermore, the spin polarization around the azide ligand is much smaller in CASSCF, while both hybrid and non-hybrid exchange–correlation functionals predict a greater excess of β-electron density around the nitrogen atoms. However, the BP86, BLYP, and PBE exchange–correlation functionals result in magnetization densities that appear qualitatively closest to the CAS(15,11)SCF reference distribution, with the smallest amount of β-electron density around the nitrogen atoms.

The absolute error and root-square error for all DFT–CASSCF magnetization density difference distributions are summarized in Table 1. As observed for compound **1**, the meta-GGA functionals (PBE, BP86, OLYP, OPBE, and BLYP) have the largest Δ_{abs} and Δ_{rs} values for all investigated exchange–correlation functionals, despite their qualitative agreement in magnetization densities with the CASSCF reference distribution. For complex **2**, the smallest errors are found for the PBE0 and B3LYP exchange–correlation functionals, even though the corresponding magnetization densities differ qualitatively more from the CASSCF reference. We should note that, for complex **2**, all hybrid exchange–correlation functionals predict magnetization densities that have the smallest Δ_{abs} and Δ_{rs} errors for all investigated exchange–correlation functionals.

3.1.3 Complex 3—Nitrosyl.

The magnetization density distributions of complex **3** are shown in Figure 2(c), but with an isosurface value of 0.003. Similar to compounds **1** and **2**, all CASSCF calculations result in similar magnetization density distributions. The differences between CAS(6,6)SCF, CAS(8,8)SCF, and CAS(10,12)SCF are negligible and much smaller than the differences between CASSCF and DFT (see Table 1 and Supplementary Figures S14 and S16). Thus, only the CAS(10,12)SCF result is shown in Figure 2. As for compounds **1** and **2**, an analysis of the CASSCF wavefunction indicates a single-reference nature of system **3** (large (absolute) CI expansion coefficients of the principal configuration of 0.95 and $|\mathrm{CI}|^2 = 0.91$).

In contrast to **1** and **2**, the α-electron density on **3** primarily resides on the C-C-N-C-C ligand backbone for both DFT and CASSCF (see Figure 2(c) and Supplementary Figure S15). Most importantly, CASSCF predicts no β-electron density on the ligand backbone, whereas all exchange–correlation functions show various amounts of β-electron density, depending on the exchange–correlation functional, including a larger excess of β-electron density on the iridium center. Furthermore, the α-electron density on the nitrosyl ligand is much smaller in CASSCF results compared to DFT. The main difference between the hybrid exchange–correlation functionals, such as B3LYP, and the other exchange–correlation functionals, such as BP86, is that the hybrid functionals have a larger excess of β-electron density around the iridium atom and the pincer ligand. This small amount of β-electron density present on complex **3** for the BP86, BLYP, and PBE exchange–correlation functionals results in a closer comparison to the CAS(10,12)SCF results, as seen from the DFT–CASSCF difference plots (Supplementary Figure S16).

Furthermore, the absolute error and root-square error for all DFT–CASSCF magnetization density difference distributions are smallest for all meta-GGA functionals (see Table 1), with BP86, BLYP, and PBE deviating least from the CASSCF reference. In contrast to **1** and **2**, hybrid exchange–correlation functionals yield the largest Δ_{abs} and Δ_{rs} errors. These errors are reflected in the large differences in magnetization density around the iridium metal center and the nitrosyl ligand (see also Figure S16 of the Supplementary Information).

3.1.4 Concluding remarks.

For all investigated complexes **1** to **3**, the DFT magnetization densities are more strongly delocalized on the ligand atoms and the PNP pincer-type ligand backbone than the corresponding CASSCF magnetization densities. Moreover, all approximate exchange–correlation functionals predict more spin-polarized systems where non-vanishing amounts of β-electron density are distributed over the ligand atoms (axial ligands and the pincer ligand) and the metal center (see also Figure 2). In general, all investigated exchange–correlation functionals yield qualitatively different magnetization density distributions compared to CASSCF, with results obtained by non-hybrid exchange–correlation functionals, in particular BP86, being qualitatively closest to the CASSCF reference data. However, looking at the Δ_{abs} and Δ_{rs} errors with respect to the CASSCF reference distribution, it remains ambiguous which exchange–correlation functionals can accurately predict the magnetization density in the investigated iridium compounds. While both hybrid and non-hybrid functionals perform similar for compound **1**, smaller Δ_{abs} and Δ_{rs} errors are found for hybrid functionals for complex **2** and non-hybrid functionals for complex **3**, respectively. We should emphasize that the largest errors are obtained for complex **3**, irrespective of the approximate exchange–correlation functional.

Furthermore, when the ligand in iridium PNP pincer-type complexes is changed from nitrido, to azide, and to nitrosyl, the α-electron density is shifted from the N atom of the nitrido ligand, over the iridium metal center, to the PNP pincer ligand of complex **3**. Specifically, while the α-electron density is equally localized on the nitrido ligand and the metal center in complex **1**, compound **2** features an excess of α-electron density mainly on the metal center. Substituting the azide ligand by a nitrosyl group shifts the spin density almost completely on the amido-backbone. Therefore, in accordance with the decrease in magnetization density (excess of α-electron density) on the metal center in compound **3**, its reactivity decreases compared to the reactivity of **1** and **2**.[70]

Table 2 g tensors for compounds **1**, **2**, and **3** determined by the BP86 and B3LYP exchange–correlation functional. Experimental data, if available, is provided for comparison. Δg: g anisotropy.

Complex	BP86				B3LYP				experiment[21]			
	g_{11}	g_{22}	g_{33}	Δg	g_{11}	g_{22}	g_{33}	Δg	g_{11}	g_{22}	g_{33}	Δg
1	1.521	1.896	2.065	0.544	1.354	1.848	2.011	0.657	1.320	1.631	1.885	0.565
2	1.924	2.162	2.900	0.976	1.837	2.137	3.241	1.404	–	–	–	–
3	1.979	1.988	2.000	0.021	1.936	1.984	1.995	0.059	–	–	–	–

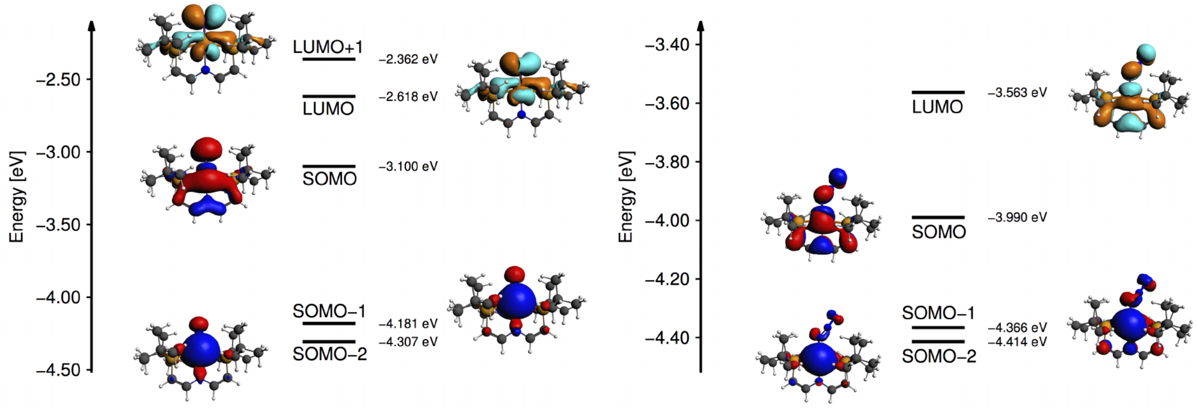

(a) **1** (b) **2**

Fig. 3 Valence energy levels of a) complex **1** and b) complex **2** determined from the BP86 exchange–correlation functional using the spin-orbit ZORA Hamiltonian.

3.2 Magnetic properties

The magnetization density distributions discussed in the previous section allow for a qualitative analysis of the differences between CASSCF and DFT calculations and their optimized electronic structures. To emphasize the differences between various exchange–correlation functionals, we have determined the magnetic properties of all iridium compounds, which will facilitate a quantitative comparison between different exchange–correlation functionals. In EPR spectroscopy,[71] the g tensor is a global property of the molecule as it depends (among other things) on the distribution of the unpaired electron which may be delocalized over substantial parts of the molecular system. Furthermore, the interaction of the unpaired electrons with nuclear magnetic moments gives rise to the phenomenon of hyperfine coupling which provides valuable information about the electronic structure of the molecule.

Tables 2 and 3 summarize the molecular g tensor and the A tensor of selected atoms for compounds **1**, **2**, and **3** and the BP86 and B3LYP exchange–correlation functionals as well as experimental results for the compounds that are available. While complex **1** and **2** have g value components larger than 2.1 and smaller than 1.95, respectively, indicating that the radical is mostly centered on the metal atom, compound **3** features g values that are close to 2.0 suggesting that the (unpaired electron) spin density is distributed over the ligand atoms.[72] Similarly, the large g anisotropy Δg found for compound **1** and **2** points to a large amount of spin density localized on the metal center, whereas the negligibly small Δg value for complex **3** denotes an excess of spin density on the ligand backbone (*cf*. magnetization density distributions shown in Figure 2). Specifically, Δg is considerably larger for compound **2** than for complex **1**, suggesting a larger amount of spin density on the metal center and thus supporting the previously observed shift in α-electron density from the axial ligand to the iridium center when changing the nitrido ligand to an azide ligand. Comparing to experimental data for compound **1**, we can conclude that none of the studied exchange–correlation functionals is able to predict an accurate g tensor, whose components are, in general, overestimated in DFT calculations. Specifically, BP86 yields a Δg that agrees well with the experimental value, while the components of the g tensor calculated by B3LYP are closer to the experimentally determined ones. Finally, we should note that despite the large atomic number of the iridium atom,[73] the effect of spin–orbit coupling is small, usually in the range of 0.1 to 0.5 eV for the Ir $5d$−shell,[73] similar to other $5d$ metal complexes containing anion radicals.[74]

Furthermore, the differences in electronic structure are reflected in the different values of the g tensor. For compound **1**, the components of g are in general smaller than 2 which indicates that the Singly Occupied Molecular Orbital (SOMO) lies energetically closer to the Lowest Unoccupied MO (LUMO). In contrast to **1**, the components of g for compound **2** are generally larger than 2 suggesting that the SOMO is energetically closer to the Highest Occupied MO (HOMO) than to the LUMO (see also Figure 3). We should note that although the overall trends in g tensors are similar for BP86 and B3LYP, both exchange–correlation functionals yield considerably different components of the g tensor for all investigated iridium complexes. In general, B3LYP yields g values that deviate more strongly from 2 as well as larger g anisotropies

Table 3 A tensors (in MHz) for compounds **1**, **2**, and **3** determined by the BP86 and B3LYP exchange–correlation functional. Experimental data, if available, is provided for comparison.

	Atom	BP86			B3LYP			experimental[21]		
		a_{11}	a_{22}	a_{33}	a_{11}	a_{22}	a_{33}	a_{11}	a_{22}	a_{33}
1	Ir	−51.3	−37.9	40.7	−65.5	−44.4	34.2	–	–	–
	N2	−61.4	−17.8	50.7	−73.3	−13.7	22.1	−62.0	−26.5	63.5
2	Ir	−8.6	0.0	93.3	−29.7	−14.7	12.5	–	–	–
	N2	−2.7	−2.0	6.7	−1.8	−1.3	5.0	–	–	–
	N3	−2.7	1.1	5.6	−1.0	2.0	3.0	–	–	–
	N4	−4.6	−3.7	−1.3	−5.0	−4.8	−1.6	–	–	–
3	Ir	−13.5	−2.2	2.6	−13.1	7.1	1.8	–	–	–
	N2	2.7	4.8	19.8	3.9	6.5	26.5	–	–	–
	O	10.5	6.2	−32.4	9.81	2.0	−47.8	–	–	–

Δg. Specifically, B3LYP results in Δg values that are more than twice as large as the BP86 values. This significant discrepancy indicates that there is a larger amount of spin density located on the metal center obtained in B3LYP calculations compared to the BP86 results.

Similar trends can be observed for the A tensors. While the hyperfine couplings are large for the iridium metal center and the nitrido ligand in complex **1**, which is in agreement with the distribution of the spin density, only the metal center features a significant hyperfine coupling for complex **2** (note the small values of the A tensor for all nitrogen atoms of the azide ligand in Table 3). As expected for complex **3**, the hyperfine coupling on the metal center further decreases. However, the nitrogen and oxygen atoms of the nitrosyl ligand have non-vanishing hyperfine coupling constants which can be explained by the non-vanishing spin density on the nitrosyl ligand as predicted in all DFT calculations. As observed for g tensors and Δg, the hybrid B3LYP exchange–correlation functional yields considerably larger hyperfine couplings than BP86. Furthermore, the A tensor predicted by the BP86 exchange–correlation functional agrees very well with experimental data, while B3LYP performs better for the g tensor. We should, however, emphasize that the components of the A tensor are more sensitive to the choice of the exchange–correlation functional than the g tensor. Although the (qualitative) differences in DFT magnetization density distributions might be hardly visible from the isosurface plots, the numerical discrepancies in magnetic properties illustrate the quantitative differences between various exchange–correlation functionals in predicting electronic structures and properties for iridium complexes.

4 Conclusions

As the magnetization density is an essential quantity for the calculation of EPR parameters, quantum chemistry must be able to predict magnetization density distributions accurately. Recent studies, however, demonstrate the difficulty in calculating reliable magnetization density distributions for open-shell iron-containing complexes.[23,33,34] Specifically, magnetization density distributions strongly depend on the chosen approximate exchange–correlation functional. In this work, we have investigated the performance of different exchange–correlation functionals in predicting magnetization densities and magnetic properties for iridium PNP pincer-type complexes containing different (non-innocent) ligands. Furthermore, we have studied how the magnetization density and magnetic properties change with respect to the choice of the (non-innocent) ligand.

Our study emphasizes that magnetization density distributions of iridium PNP pincer-type complexes are sensitive to the chosen approximate exchange–correlation functional. Although these discrepancies are small and less pronounced than in $3d$-transition metal complexes,[23,33] the quantitative differences in magnetic properties are non-negligible. This precludes the calculation of properties depending on the magnetization density such as EPR parameters using current approximations to the exact exchange–correlation functional.

To decide which approximate exchange–correlation functionals yield reliable magnetization density distributions, wavefunction-based methods are required. Comparison to CASSCF results can serve as an accurate benchmark of exchange–correlation functionals and highlight the most important discrepancies. We have studied different sizes of the active orbital space to ensure convergence of the magnetization density with respect to the dimension of the active space. Specifically, our CASSCF calculations indicate that the active spaces of the investigated iridium complexes are stable and that a medium-sized number of active electrons and orbitals is sufficient to describe their electronic structures reliably.

A comparison of DFT and CASSCF magnetization density isosurface plots and the absolute and square-root errors in DFT–CASSCF magnetization density difference distributions indicate that none of the investigated exchange–correlation functionals can accurately predict the magnetization density in iridium PNP pincer-type complexes. Specifically, DFT tends to distribute the spin density on the ligand atoms and the PNP backbone and predicts a large excess of β-electron density on the metal center and the ligand backbone. Although the BP86, BLYP, and PBE exchange–correlation functionals result in magnetization densities that are qualitatively closest to the CASSCF reference distribution for all investigated exchange–correlation functionals and iridium compounds, the qualitative differences around the PNP pincer backbone and around the iridium center are non-negligible. Moreover, the absolute and square-root errors in DFT–CASSCF magnetization density difference distributions highlight the ambiguity of DFT results and the difficulty in predicting both quantitatively and qualitatively accurate magnetization densities within DFT. While both hybrid and non-hybrid functionals yield similar absolute and square-root errors for compound **1**, hybrid functionals result in smaller errors for complex **2**, whereas non-hybrid functionals deviate least from the CASSCF reference for complex **3**.

Furthermore, the excess of α-electron density is strongly dependent on the choice of the non-innocent ligand and thus determines the reactivity of the corresponding iridium compounds. While the α-electron density is localized on the nitrido ligand and the iridium center in complex **1**, exchanging the nitrido ligand with the azide ligand leads to an excess of α-electron density mainly distributed over the metal center. In contrast to nitrido and azide, the nitrosyl ligand results in an iridium PNP pincer-type complex where the magnetization density is distributed over the PNP pincer backbone.

In summary, we find that none of the tested exchange–correlation functionals is able to provide a satisfactory description of the magnetization densities and magnetic properties in the investigated iridium complexes. Similar problems have been already observed for iron complexes containing non-innocent ligands.[23,33,34] In contrast to previous findings,[24] however, conventional electron correlation methods, like CASSCF, are sufficient in describing the electronic structure of the considered iridium compounds accurately. Our study emphasized the importance of analyzing density functionals to understand their failures and weaknesses and to improve current approximations to the exchange–correlation functional to be applicable to challenging problems in transition-metal chemistry. This can be achieved by, for instance, including large transition metal compounds in the test sets when developing new exchange–correlation functionals,[75] using composite approaches,[76–78] taking the magnetization density properly into account within a spin-DFT formalism,[79] and explicitly reconstructing exchange–correlation potentials from accurate (magnetization) densities[80,81] or reduced density matrices.[82]

5 Acknowledgements

We gratefully acknowledge financial support from the Natural Sciences and Engineering Research Council of Canada. K.B. acknowledges the financial support from the Swiss National Science Foundation (P2EZP2 148650), the Banting Postdoctoral Fellowship, and the National Science Center Poland, Grant No. DEC-2013/11/B/ST4/00771. P.T. thanks the National Science Center Poland, Grant Nos. DEC-2012/07/B/ST4/01347 and DEC-2013/11/B/ST4/00771.

The authors acknowledge support for computational resources from SHARCNET, a partner consortium in the Compute Canada national HPC platform.

References

1 R. A. Eikey and M. M. Abu-Omar, *Coord. Chem. Rev.*, 2003, **243**, 83–124.
2 J. Schöffel, A. Y. Rogachev, S. DeBeer George and P. Burger, *Angew. Chem.*, 2009, **121**, 4828–4832.
3 J. F. Berry, *Comments Inorg. Chem.*, 2009, **30**, 28–66.
4 B. Askevold, J. T. Nieto, S. Tussupbayev, M. Diefenbach, E. Herdtweck, M. C. Holthausen and S. Schneider, *Nat. Chem.*, 2011, **3**, 532–537.
5 J. Hohenberger, K. Ray and K. Meyer, *Nat. Commun.*, 2012, **3**, 720.
6 T. A. Betley and J. C. Peters, *J. Am. Chem. Soc.*, 2004, **126**, 6252–6254.
7 X. Shan and L. Q. Jr., *J. Inorg. Biochem.*, 2006, **100**, 421–433.
8 M. P. Mehn and J. C. Peters, *J. Inorg. Biochem.*, 2006, **100**, 634–643.
9 J.-U. Rohde, T. A. Betley, T. A. Jackson, C. T. Saouma, J. C. Peters and L. Que, *Inorg. Chem.*, 2007, **46**, 5720–5726.
10 R. Noyori and T. Ohkuma, *Angew. Chem. Int. Ed.*, 2001, **40**, 40–73.
11 J. Zhang, G. Leitus, Y. Ben-David and D. Milstein, *Angew. Chem. Int. Ed.*, 2006, **45**, 1113–1115.
12 W. S. Knowles and R. Noyori, *Acc. Chem. Res.*, 2007, **40**, 1238–1239.
13 B. Gnanaprakasam, J. Zhang and D. Milstein, *Angew. Chem. Int. Ed.*, 2010, **49**, 1468–1471.
14 R. Langer, G. Leitus, Y. Ben-David and D. Milstein, *Angew. Chem.*, 2011, **123**, 2168–2172.
15 E. Balaraman, Y. Ben-David and D. Milstein, *Angew. Chem. Int. Ed.*, 2011, **50**, 11702–11705.
16 E. Fogler, E. Balaraman, Y. Ben-David, G. Leitus, J. Shimon, Linda and D. Milstein, *Organometallics*, 2011, **30**, 3826–3833.
17 G. Zhang, B. L. Scott and S. K. Hanson, *Angew. Chem. Int. Ed.*, 2012, **51**, 12102–12106.
18 S. S. Rozenel, R. Padilla, C. Camp and J. Arnold, *Chem. Commun.*, 2014, **50**, 2612–2614.
19 M. Vogt, A. Nerush, M. A. Iron, G. Leitus, Y. Diskin-Posner, L. J. Shimon, Y. Ben-David and D. Milstein, *J. Am. Chem. Soc.*, 2013, **135**, 17004–17018.
20 J. Meiners, M. G. Scheibel, M.-H. Lemée-Cailleau, S. A. Mason, M. B. Boeddinghaus, T. F. Fässler, E. Herdtweck, M. M. Khusniyarov and S. Schneider, *Angew. Chem. Int. Ed.*, 2011, **50**, 8184–8187.
21 M. G. Scheibel, B. Askevold, F. W. Heinemann, E. J. Reijerse, B. de Bruin and S. Schneider, *Nat. Chem.*, 2012, **4**, 552–558.
22 M. G. Scheibel, Y. Wu, A. C. StuÌĹckl, L. Krause, E. Carl, D. Stalke, B. de Bruin and S. Schneider, *J. Am. Chem. Soc.*, 2013, **135**, 17719–17722.
23 K. Boguslawski, C. R. Jacob and M. Reiher, *J. Chem. Theory Comput.*, 2011, **7**, 2740–2752.
24 K. Boguslawski, K. H. Marti, Ö. Legeza and M. Reiher, *J. Chem. Theory Comput.*, 2012, **8**, 1970–1982.
25 L. Freitag, S. Knecht, S. F. Keller, M. G. Delcey, F. Aquilante, T. B. Pedersen, R. Lindh, M. Reiher and L. Gonzalez, *Phys. Chem. Chem. Phys.*, 2015, **17**, 14383–14392.
26 Y. Jiang and H. Berke, in *Nitrosyl Complexes in Inorganic Chemistry, Biochemistry and Medicine I*, Springer, 2014, pp. 167–228.
27 M. Reiher, *CHIMIA*, 2009, **63**, 140–145.
28 K. Pierloot, *Int. J. Quantum Chem.*, 2011, **111**, 3291–3301.
29 M. Reiher, O. Salomon and B. A. Hess, *Theor. Chem. Acc.*,

2001, **107**, 48.

30 O. Salomon, M. Reiher and B. A. Hess, *J. Chem. Phys.*, 2002, **117**, 4729–4737.

31 J. N. Harvey, in *Principles and Applications of Density Functional Theory in Inorganic Chemistry I*, Springer Berlin Heidelberg, 2004, vol. 112, pp. 151–184.

32 J. N. Harvey, *Annu. Rep. Prog. Chem., Sect. C: Phys. Chem.*, 2006, **102**, 203–226.

33 J. Conradie and A. Ghosh, *J. Phys. Chem. B*, 2007, **111**, 12621–12624.

34 A. Ghosh, *J. Biol. Inorg. Chem.*, 2006, **11**, 712–724.

35 C. J. Cramer and D. G. Truhlar, *Phys. Chem. Chem. Phys.*, 2009, **11**, 10757–10816.

36 H. Paulsen, V. Schünemann and J. A. Wolny, *Eur. J. Inorg. Chem.*, 2013, **2013**, 628–641.

37 K. Boguslawski and M. Reiher, in *Chemical Bonding in Open-Shell Transition-Metal Complexes*, Wiley-VCH, 2014, pp. 219–252.

38 A. J. Cohen, P. Mori-Sánchez and W. Yang, *Science*, 2008, **321**, 792–794.

39 A. J. Cohen, P. Mori-Sánchez and W. Yang, *Chem. Rev.*, 2012, **112**, 289.

40 J. P. Perdew, M. Ernzerhof, K. Burke and A. Savin, *Int. J. Quantum Chem.*, 1997, **61**, 197–205.

41 P. Mori-Sánchez, A. J. Cohen and W. T. Yang, *J. Chem. Phys.*, 2006, **125**, 201102.

42 A. Ruzsinszky, J. P. Perdew, G. I. Csonka, O. A. Vydrov and G. E. Scuseria, *J. Chem. Phys.*, 2007, **126**, 104102.

43 A. J. Cohen, P. Mori-Sánchez and W. Yang, *J. Chem. Phys.*, 2008, **129**, 121104.

44 R. Haunschild, T. M. Henderson, C. A. JimÃĺnez-Hoyos and G. E. Scuseria, *J. Chem. Phys.*, 2010, **133**, 134116.

45 G. te Velde, F. M. Bickelhaupt, S. J. A. van Gisbergen, C. F. Guerra, E. J. Baerends, J. G. Snijders and T. Ziegler, *J. Comput. Chem.*, 2001, **22**, 931–967.

46 J. P. Perdew, *Phys. Rev. B*, 1986, **33**, 8822.

47 A. Becke, *Phys. Rev. A*, 1988, **38**, 3098.

48 E. van Lenthe, E. J. Baerends and J. G. Snijders, *J. Chem. Phys.*, 1993, **99**, 4597.

49 A. D. Becke, *J. Chem. Phys.*, 1993, **98**, 5648–5653.

50 C. Lee, W. Yang and R. G. Parr, *Phys. Rev. B*, 1988, **37**, 785.

51 Y. Zhao and D. G. Truhlar, *J. Chem. Phys.*, 2006, **125**, 13126.

52 Y. Zhao and D. G. Truhlar, *Acc. Chem. Res.*, 2008, **41**, 157.

53 N. C. Handy and A. J. Cohen, *Mol. Phys.*, 2001, **99**, 403–412.

54 J. P. Perdew, K. Burke and M. Ernzerhof, *Phys. Rev. Lett.*, 1996, **77**, 3865.

55 C. Adamo and V. Barone, *J. Chem. Phys.*, 1999, **110**, 6158–6170.

56 M. Ernzerhof and G. Scuseria, *J. Chem. Phys.*, 1999, **110**, 5029.

57 J. Tao, J. P. Perdew, V. N. Staroverov and G. E. Scuseria, *Phys. Rev. Lett.*, 2003, **91**, 146401.

58 V. N. Staroverov, G. E. Scuseria, J. Tao and J. P. Perdew, *J. Chem. Phys.*, 2003, **119**, 12129–12137.

59 E. van Lenthe, P. E. S. Wormer and A. van der Avoird, *J. Phys. Chem.*, 1997, **107**, 2488—-2498.

60 E. van Lenthe, A. van der Avoird and P. E. S. Wormer, *J. Phys. Chem.*, 1998, **108**, 4783.

61 B. Roos and P. R. Taylor, *Chem. Phys.*, 1980, **48**, 157–173.

62 H.-J. Werner and P. J. Knowles, *J. Chem. Phys.*, 1985, **82**, 5053–5063.

63 P. J. Knowles and H.-J. Werner, *Chem. Phys. Lett.*, 1985, **115**, 259–267.

64 H.-J. Werner, P. J. Knowles, R. q, F. R. Manby, P. C. M. Schütz, T. Korona, A. Mitrushenkov, G. Rauhut, T. B. Adler, R. D. Amos, A. Bernhardsson, A. Berning, D. L. Cooper, M. J. O. Deegan, A. J. Dobbyn, F. Eckert, E. Goll, C. Hampel, G. Hetzer, T. Hrenar, G. Knizia, C. Köppl, Y. Liu, A. W. Lloyd, R. A. Mata, A. J. May, S. J. McNicholas, W. Meyer, M. E. Mura, A. Nicklass, P. Palmieri, K. Pflüger, R. Pitzer, M. Reiher, U. Schumann, H. Stoll, A. J. Stone, R. Tarroni, T. Thorsteinsson, M. Wang and A. Wolf, *MOLPRO, Version 2010.1, A Package Of* Ab Initio *Programs*, 2012, see http://www.molpro.net.

65 P.-O. Widmark, P.-A. Malmqvist and B. O. Roos, *Theor. Chim. Acta*, 1990, **77**, 291–306.

66 B. O. Roos, R. Lindh, P.-A. Malmqvist, V. Veryazov and P.-O. Widmark, *J.Phys. Chem. A*, 2004, **108**, 2851–2858.

67 B. O. Roos, R. Lindh, P.-A. Malmqvist, V. Veryazov and P.-O. Widmark, *J. Phys. Chem. A*, 2005, **109**, 6575–6579.

68 M. Douglas and N. Kroll, *Ann. Phys.*, 1974, **82**, 89.

69 B. A. Hess, *Phys. Rev. A*, 1986, **33**, 3742.

70 M. Lazar, V. Klimo, J. Rychly, P. Pelikan and L. Valko, *Free Radicals in Chemistry and Biology*, CRC Press, Boca Raton, 1989.

71 M. Kaupp, M. Bühl and V. G. Malkin, *Calculation of NMR and EPR Parameters: Theory and Applications*, John Wiley & Sons, 2006.

72 B. De Bruin, D. G. H. Hetterscheid, A. J. J. Koekkoek and H. Grützmacher, in *The Organometallic Chemistry of Rh-, Ir-, Pd-, and Pt-Based Radicals: Higher Valent Species*, John Wiley & Sons, Inc., 2008, pp. 247–354.

73 I. V. Khudyakov, Y. A. Serebrennikov and N. J. Turro, *Chem. Rev.*, 1993, **93**, 537–570.

74 P. Singh, *Ph.D. thesis*, Stuttgart University, 2008.

75 T. Weymuth, E. P. A. Couzijn, P. Chen and M. Reiher, *J. Chem. Theory Comput.*, 2014, **10**, 3092–3103.

76 N. J. DeYonker, K. A. Peterson, G. Steyl, A. K. Wilson and T. R. Cundari, *J. Phys. Chem. A*, 2007, **111**, 11269–11277.

77 S. Li, J. M. Hennigan, D. A. Dixon and K. A. Peterson, *J. Phys. Chem. A*, 2009, **113**, 7861–7877.

78 W. Jiang, M. L. Laury, M. Powell and A. K. Wilson, *J. Chem. Theory Comput.*, 2012, **8**, 4102–4111.

79 C. R. Jacob and M. Reiher, *Int. J. Quantum Chem.*, 2012, **112**, 3661–3684.

80 C. R. Jacob, *J. Chem. Phys.*, 2011, **135**, 244102.

81 K. Boguslawski, C. R. Jacob and M. Reiher, *J. Chem. Phys.*, 2013, **138**, 044111.

82 I. G. Ryabinkin, S. V. Kohut and V. N. Staroverov, *Phys. Rev.*

Lett., 2015, **115**, 083001.